Revealing photovoltaic behavior in 2D hybrid perovskite ferroelectric single-crystalline microwire arrays for self-powered photodetectors

Ran Ding [a], Yongxin Lyu [a], Yuqian Zhao [a], Zehan Wu [a], Feng Guo [a], Weng Fu Io [a], Sin-Yi Pang [a], Jianfeng Mao [a], Man-Chung Wong [a], Lok Wing Wong [a], Cenqi Yan [b], Jiangsheng Yu [b], Jiong Zhao [a], Gang Li [b], Jianhua Hao [a,*]

[a] Department of Applied Physics, The Hong Kong Polytechnic University, Hung Hom, Hong Kong, PR China
[b] Department of Electronic and Information Engineering, The Hong Kong Polytechnic University, Hung Hom, Hong Kong, PR China

ARTICLE INFO

ABSTRACT

Hybrid perovskite ferroelectrics produce a revival of interest in ferroelectric photovoltaics because of the robust ferroelectricity coexisting with superior semiconducting properties. An electric field via perovskite ferroelectrics can affect their photovoltaic behavior; however, the fundamental understanding of the electric-field-induced effects remains comparatively elusive. Herein, $(EA)_2(MA)_2Pb_3Br_{10}$ single-crystalline microwire arrays (MWs) are synthesized for the fabrication of self-powered photodetectors and characterized with evident in-plane multiaxial ferroelectricity by piezoresponse force microscopy (PFM) measurements. Upon systematic investigations via a dynamic poling process, including electrical-poling-dependent photocurrent, Kelvin probe force microscopy (KPFM) mapping and ferroelectric polarization switching, we reveal that the coupling of ion migration and ferroelectric photovoltaic effect dominate the photovoltaic behavior within $(EA)_2(MA)_2Pb_3Br_{10}$ MWs. Such electric-field-induced effects are responsible for the self-powered ability in $(EA)_2(MA)_2Pb_3Br_{10}$ MWs-based photodetectors with accelerated response time, switchable photoelectric responses and large short-circuit current density. Our findings provide fundamental insight into the photovoltaic behavior under an electric field in perovskite ferroelectrics, and the electrical-poling-manipulated dynamics pave the way for innovative self-powered optoelectronic devices.

1. Introduction

The discovery of ferroelectric photovoltaics can date back to the 1970s, which has been extensively exploited in a variety of ferroelectric materials [1–3]. Unlike conventional junction solar cells, a steady-state photovoltaic response can be generated along the ferroelectric polarization direction due to the strong inversion symmetry breaking. Such a unique mechanism endows ferroelectric photovoltaics with several exceptional properties, such as switchable photoelectric responses, above-bandgap photovoltage, and polarization-dependent activity, which are especially attractive for the applications of solar cells, photodetectors and self-powered electronics [4–10]. Unfortunately, the prototypical ferroelectric materials such as perovskite oxides still suffer from wide bandgaps (2.7–5 eV) that lead to the limitation of absorbing solar spectrum with only 8–20%. Their further advancement in solar cells is hindered by their relatively low power conversion efficiency and

photocurrent density in the order of $\sim$nA cm^{-2}. In this context, the search and design of a new system of ferroelectrics is put on the agenda that should encompass suitable bandgaps in the visible regions and enable efficient photovoltaic outputs.

In recent years, hybrid perovskites have attracted tremendous attention due to their superior semiconducting properties that are promising for photovoltaic applications [11–14]. Benefiting from their structural flexibility, the family of hybrid perovskites can be enriched with a broad diversity and versatile functionalities through rational design and compositional engineering. Among them, Ruddlesden-Popper (RP)-type 2D perovskites as a vital subset have a general formula of $R_2A_{n-1}B_nX_{3n+1}$, where both R and A are organic cations, B is metal anion, X is halogen, and n determines the layer number of inorganic frameworks [15–17]. Relaxing from the Goldschmidt's tolerance factor, long-chain alkylammonium spacer cation (R) is allowed to be adopted into perovskite layered metal-halide slabs,

---

which may result in the inversion symmetry breaking and therefore favor the generation of ferroelectricity inside hybrid perovskites. Nowadays, 2D perovskite ferroelectrics have emerged as a new branch of ferroelectrics that show great appeal in the field of ferroelectric photovoltaics for their robust ferroelectricity containing high spontaneous polarization, tunable bandgap and multiaxial features, as well as excellent photoexcitation and semiconducting characteristics [18–22]. Switchable photoelectric responses in self-powered photodetectors based on 2D perovskite ferroelectrics have been observed, and can be ascribed to the separation and flipping of polarization-related photoexcited carries [23–27]. From the structural viewpoint, polarization switching arises from the dynamic reorientation of bulky organic cations combined with the tilting motions of inorganic frameworks.

Significantly, ion migration effects have been identified as the intrinsic property of hybrid perovskites, having a strong influence on the device operation [28–31]. Analyses reveal that ion migration of cations or anions enables to induce p- and n-type doping in the vicinity of electrodes, thus yielding a flipped p-i-n structure after an inverting electrical poling. As suggested by the experimental evidence, the ion migration is speculated to be an important contributing factor for those unusual observations, such as photocurrent-voltage hysteresis, photoinduced self-poling effect and switchable photovoltaic effect, which are analogous to the ferroelectric photovoltaic effect. However, for perovskite ferroelectrics with robust ferroelectricity, whether ion migration would also affect the photovoltaic behavior remains largely unknown. The in-depth understanding of these electric-field-induced effects is necessary, since it might provide hints for the development of novel ferroelectric photovoltaics and also expand hybrid perovskite ferroelectrics for self-powered electronics.

In this work, high-quality $(EA)_2(MA)_2Pb_3Br_{10}$ MWs were utilized and fabricated through a template-assisted space-confined method. Their in-plane ferroelectric nature is investigated by PFM measurements, exhibiting randomly distributed domains with multiaxial domain textures. Impressive photodetection performance is obtained from the photodetectors based on $(EA)_2(MA)_2Pb_3Br_{10}$ MWs with a high responsivity of 415 mA W^{-1} and detectivity of 3.23×10^{12} cm $Hz^{1/2}$ W^{-1}. After an electrical poling, $(EA)_2(MA)_2Pb_3Br_{10}$ MWs-based photodetectors exhibit an obvious self-powered ability with accelerated response time, switchable photoelectric responses and large short-circuit current density. Systematic investigations, including electrical-poling-dependent photocurrent, KPFM mapping and ferroelectric polarization switching, are further carried out to reveal the photovoltaic behavior via a dynamic poling process. Upon a high-electric-field poling, the electric field is able to trigger ion migration and polarization switching within $(EA)_2(MA)_2Pb_3Br_{10}$ MWs, thus inducing space-charge doping and aligning the ferroelectric polarization, assessed by KPFM and PFM measurements. Consequently, the coupling of ion migration and ferroelectric photovoltaic effect is confirmed to be responsible for the photovoltaic behavior in perovskite ferroelectrics. Our findings bring fundamental and practical insights into the electric-field-induced effects on tailoring the photovoltaic behavior in perovskite ferroelectrics, and highlight the significance of the electrical-poling-manipulated dynamics for the development of self-powered electronics with markedly improved performance.

2. Material and methods

2.1. Materials

All raw materials were purchased from the commercial supplier of Sigma-Aldrich, Inc. and used without any purification. Ethylammonium bromide (EABr, 98%), methylammonium bromide (MABr, 98%), lead bromide ($PbBr_2$, 99%), *N,N*-dimethylformamide (DMF, 99%), octadecyltrichlorosilane (OTS, ≥90%), Buffered oxide etchant (BOE, 6 : 1).

2.2. Si template fabrication

The Si template was fabricated through standard photolithography with the following steps: (1) silicon substrate with 100 nm SiO_2 layer was covered by a photoresist layer (AZ 5214 E, MicroChemicals) that was spin-coated at 3000 r/min; (2) microchannel pattern was obtained using the standard photolithography (Suss MA6 Aligner) and performed on the photoresist through a mask; (3) wet etching (Buffered oxide etchant, 6: 1, and time is 75 s) was then used to etch the SiO_2 layer and transferred the photoresist mask patterns to the Si substrate; (4) photoresist mask was completely removed in acetone, and microchannel array patterns with a period of 10 μm and 50% duty cycle were constructed on the Si template.

2.3. Growth of $(EA)_2(MA)_2Pb_3Br_{10}$ MWs

The template-assisted space-confined growth method was developed to grow $(EA)_2(MA)_2Pb_3Br_{10}$ single-crystalline microwire arrays that was described with details in Fig. S1. The precursor solution of $(EA)_2(MA)_2Pb_3Br_{10}$ (0.25 M) was prepared by dissolving EABr, MABr and $PbBr_2$ at a molar ratio of 2: 2: 3 in DMF solvent and stirring at 55 °C for 6 h. The substrates used in the growth were washed with acetone, ethanol, and deionized water in turn, and finally dried by nitrogen gas flow. The OTS-surface modification was carried out on the Si template before the growth.

2.4. Characterizations of $(EA)_2(MA)_2Pb_3Br_{10}$ MWs

The prepared $(EA)_2(MA)_2Pb_3Br_{10}$ MWs were characterized by SEM (JSM-6490, JEOL), XRD (Rigaku SmartLab), UV–Vis absorption spectra (UV-2450, Shimadzu), and UPS (Thermo Scientific Nexsa). PL spectra and time-resolved PL measurements were performed with a time-correlated single-photon counting system of the FLS920 Edinburgh spectrometer, which was equipped with a 379 nm ps diode laser to excite the samples (Edinburgh Instruments EPL-375). TEM, high-resolution TEM and EDX analysis were performed on JEM-2100F, JEOL. SHG signals were obtained from a confocal microscope (Leica Microsystems) equipped with a Ti: sapphire femtosecond laser to excite the samples at the wavelength of 1000 nm. AFM, PFM and KPFM measurements were conducted using the Asylum Research MFP-3D Infinity (Oxford Instrument). Conductive probes (Pt/Ir-coating) with different spring constants were utilized for acquiring lateral PFM (CONTPt-10, 0.2 N/m) and KPFM (EFM-20, 2.8 N/m) images. Sample surface potential can be determined by KPFM which is operating at AC mode and NAP mode with a delta height of 50 nm. Generally, the $(EA)_2(MA)_2Pb_3Br_{10}$ MWs used for PFM and KPFM measurements were grown on Pt-coated SiO_2/Si substrates in order to minimize the effects of electrostatic interactions. The dynamic poling process was carried out by applying voltage pulses to the two-terminal electrodes of photodetectors. The voltage pulses with different bias were applied for about 10 min on the devices with a 50% duty cycle and a duration of 0.1 s.

2.5. Calculations

Density functional theory calculations were performed using the plane-wave pseudopotential code Quantum Espresso (QE) [60]. The exchange and correlation energy were described by the generalized gradient approximation (GGA) with Perdew-Burke-Ernzerhof (PBE) parametrization [61]. Electron-ion interactions were described by ultrasoft pseudopotentials. Electrons from Pb 5d, 6s, 6p; N and C 2s, 2p; H 1s and Br 4s, 4p shells are explicitly included in the calculations. Plane-wave basis set cutoffs for the wave function and the electron density were set to 25 and 200 Ry, respectively. The van der Waals interaction between the organic molecules and the inorganic framework was considered by employing the DFT-D3 dispersion correction from Grimme [62]. The Brillouin-zone was sampled for integrations

according to the scheme proposed by Monkhorst-Pack [63]. K-point grid with a separation of 0.15 Å^{-1} is used. The Quantum Espresso was also employed for the Berry phase method by adding the contributions of both electrons and nuclei to calculate the spontaneous polarization of $(EA)_2(MA)_2Pb_3Br_{10}$, and the detailed computational setup was described in the reference. [42] The $(EA)_2(MA)_2Pb_3Br_{10}$ crystallographic structure used in this paper has been downloaded free of charge from the Cambridge Crystallographic Data Centre, CCDC, 12 Union Road, Cambridge CB21EZ, UK and quoted the depository numbers CCDC-1923166 (http://www.ccdc.cam.ac.uk). During the calculations, the atomic positions were fully relaxed to their equilibrium positions until there were no forces larger than 0.05 eV Å^{-1}.

2.6. Device fabrication and electrical measurements

$(EA)_2(MA)_2Pb_3Br_{10}$ MWs-based photodetectors were achieved by electron-beam deposition of a couple of Au electrodes (60 nm) onto the MW arrays through a shadow mask. The channel length and width of the photodetectors were controlled to be 50 and 250 μm, respectively, through the shadow mask. Electrical measurements were carried out by a semiconductor characterization system (Keithley 4200A-SCS) via a probe station (Lakeshore, CRX-6.5K). Monochromatic LED with a wavelength of 400 nm was used during the photodetection measurements, and a power meter (Thorlabs GmbH., PM 100D) was employed to calibrate the light intensity. The temporal response was measured via a low noise current preamplifier (Stanford Research Systems, SR570) connecting to a digital storage oscilloscope (LeCroy WaveRunner Oscilloscope, 44MXI). The LED was driven by a signal generator that can generate pulsed light at different frequencies. The noise spectrum of the photodetector was extracted by doing a Fourier transform of the dark current that was recorded by the semiconductor analyser.

3. Results and discussion

$(EA)_2(MA)_2Pb_3Br_{10}$ adopts a typical RP-type perovskite framework that consists of trilayered inorganic $[PbBr_6]^{4-}$ octahedra incorporated

with the MA$^+$ cations acting as "perovskitizer" and bulky EA$^+$ cations acting as the "spacer" between two adjacent inorganic trilayers via weak van der Waals (vdW) bonds [23–25]. As shown in Fig. 1a, $(EA)_2(MA)_2Pb_3Br_{10}$ can be regarded as a derivative of the prototype 3D MAPbBr$_3$ that is sliced into 2D layered structure by alloying of EA$^+$ cations. The complete unit cell (uc) of $(EA)_2(MA)_2Pb_3Br_{10}$ contains two perovskite trilayers with a thickness of ∼4.63 nm. The $(EA)_2(MA)_2Pb_3Br_{10}$ MWs were synthesized using a template-assisted space-confined method, which possess well-aligned structures with excellent crystallinity and controlled thickness [32–40]. Single-crystallinity with fewer grain boundaries and minimum structural defects provides adequate media to reveal the intrinsic properties of hybrid perovskites [32–36]. In addition, high crystallographic orientation of microwire arrays creates an effective in-plane exciton transporting path that can suppress undesirable scattering and trapping, and thus enjoy an active photoconductive gain [37–40]. During the fabrication, a piece of Si template with microchannel arrays was utilized to construct the confined space by imprinting the template onto a target substrate (Fig. 1b). Crystallization of $(EA)_2(MA)_2Pb_3Br_{10}$ occurred within these microchannels upon thermal evaporation of the precursor solution. The fabrication processes were schematically illustrated in Fig. S1 and described in detail. As shown in Fig. 1c, the well-aligned $(EA)_2(MA)_2Pb_3Br_{10}$ MWs have decently replicated the microstructures of Si template with lengths up to hundreds of micrometers along the lateral dimension. X-ray diffraction (XRD), scanning electron microscopy (SEM), high-resolution transmission electron microscopy (HRTEM), and selected-area electron diffraction (SAED) analyses were taken to characterize the crystallography and surface morphology of the $(EA)_2(MA)_2Pb_3Br_{10}$ MWs. A series of periodic sharp diffraction peaks in the XRD diagram can be indexed to the diffraction of the (l00) lattice planes of the 2D layered $(EA)_2(MA)_2Pb_3Br_{10}$ (Fig. 1d), which implies a single-crystalline nature with pure crystallographic orientation [24].

Moreover, the high crystallinity of the MWs was further validated by HRTEM and SAED (Fig. 1e). The corresponding SAED pattern displays sharp diffraction spots indicating a preferential growth direction of the perovskite MWs. Elemental composition of the MWs was attained from
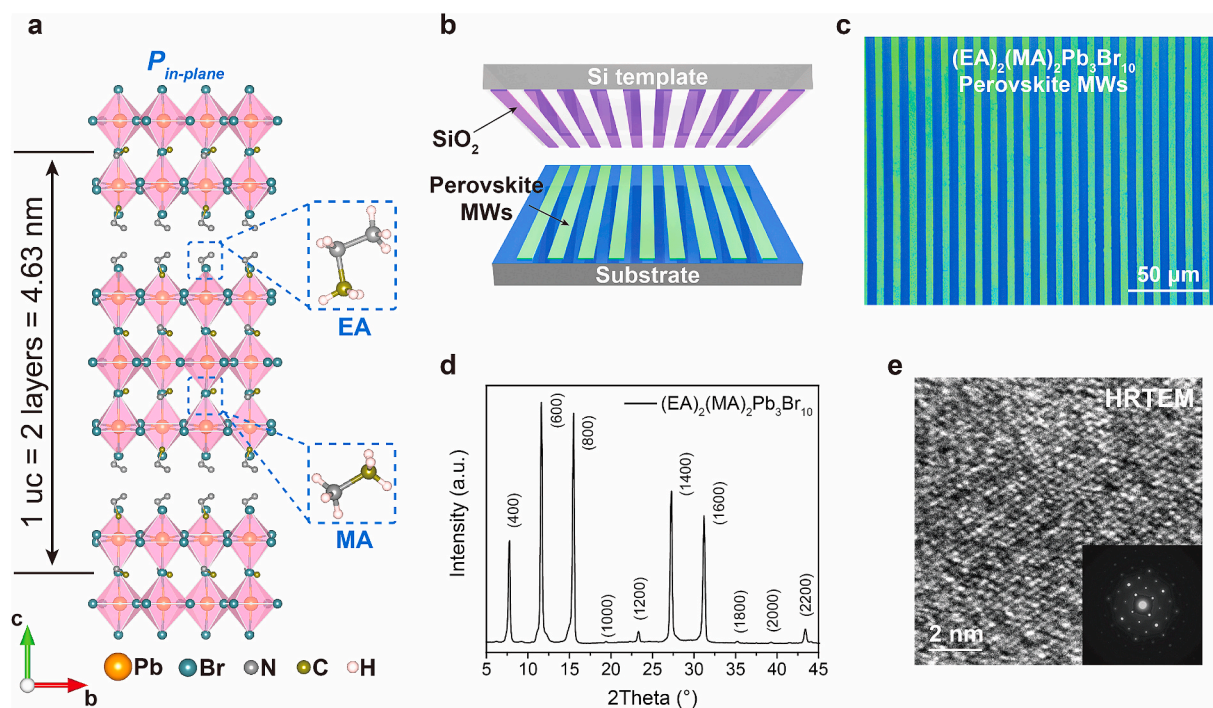

Fig. 1. (a) Perspective view of 2D perovskite $(EA)_2(MA)_2Pb_3Br_{10}$ in ferroelectric phase. EA and MA molecules are shown in an enlarged view. (b) Schematic illustration of template-assisted space-confined method for producing $(EA)_2(MA)_2Pb_3Br_{10}$ MWs. (c) Optical microscopy image, (d) XRD pattern of the $(EA)_2(MA)_2Pb_3Br_{10}$ MWs. (e) HRTEM image of the $(EA)_2(MA)_2Pb_3Br_{10}$ MWs. Inset is the corresponding SAED pattern.

the energy-dispersive X-ray spectroscopy (EDS) element mappings. The lead and bromine are readily confirmed with the atomic ratio of ~1: 2.95 (Fig. S2), which is close to the stoichiometry of $(EA)_2(MA)_2Pb_3Br_{10}$. The SEM image shown in Fig. 2a also reveals that the as-synthesized $(EA)_2(MA)_2Pb_3Br_{10}$ MWs possess uniform morphology without apparent pinholes and grain boundaries on the top surface. Atomic force microscopy (AFM) measurements reveal that our space-confined-grown microwire arrays are fabricated with stringent alignment, defined duty cycle, and controlled thickness. The AFM image and height profile of the MWs in Fig. 2b and c displays a regular height of 100 nm and a 50% duty cycle with the same width and interval length of 5 μm. The surface topography of MWs was also inspected by the root-mean-square (RMS) roughness, which exhibited a small value of 162 pm pointing to their excellent crystallinity (Fig. S3). The decent replication of the microstructures in the Si template can be further confirmed by the characterizations of the Si template, as shown in Fig. S4. By comparing the height profiles, $(EA)_2(MA)_2Pb_3Br_{10}$ MWs have fully replicated the morphologies of the Si template. In general, this template-assisted space-confined crystallization guarantees the precise control of dimension, position, and alignment for single-crystalline perovskites, which

facilitates a further step for the perovskite development with well-defined structures.

At room temperature, $(EA)_2(MA)_2Pb_3Br_{10}$ will crystallize in ferroelectric phase and exhibit a polar structure with orthorhombic space group of $Cmc2_1$, as shown in Fig. 1a [24]. Owing to the strong hydrogen bonds (N–H···Br), the MA^+ cations are tightly confined inside the corner-sharing $[PbBr_6]^{4-}$ octahedra and the bilayers of EA^+ cations are arranged head-to-tail within the vdW interlayer space. The oriented organic moieties may enhance the distortion of $[PbBr_6]^{4-}$ octahedra and greatly favor the generation of electric polarization [19,20]. Consequently, the combination of these dynamic motions destroys the superposition of the positive and negative charge centers, contributing to the non-zero spontaneous polarization of $(EA)_2(MA)_2Pb_3Br_{10}$ along the in-plane direction. As the temperature increases above its Curie temperature (393 K), $(EA)_2(MA)_2Pb_3Br_{10}$ will transform to the paraelectric state adopting a centrosymmetric tetragonal space group of $I4/mmm$ [24]. The symmetry breaking in $(EA)_2(MA)_2Pb_3Br_{10}$ meets the requirement of the Aizu notation $4/mmmFmm2$, which is one of the 88 potential ferroelectric phase transitions [41]. Accompanying the phase transition from paraelectric to ferroelectric, the number of symmetry operations
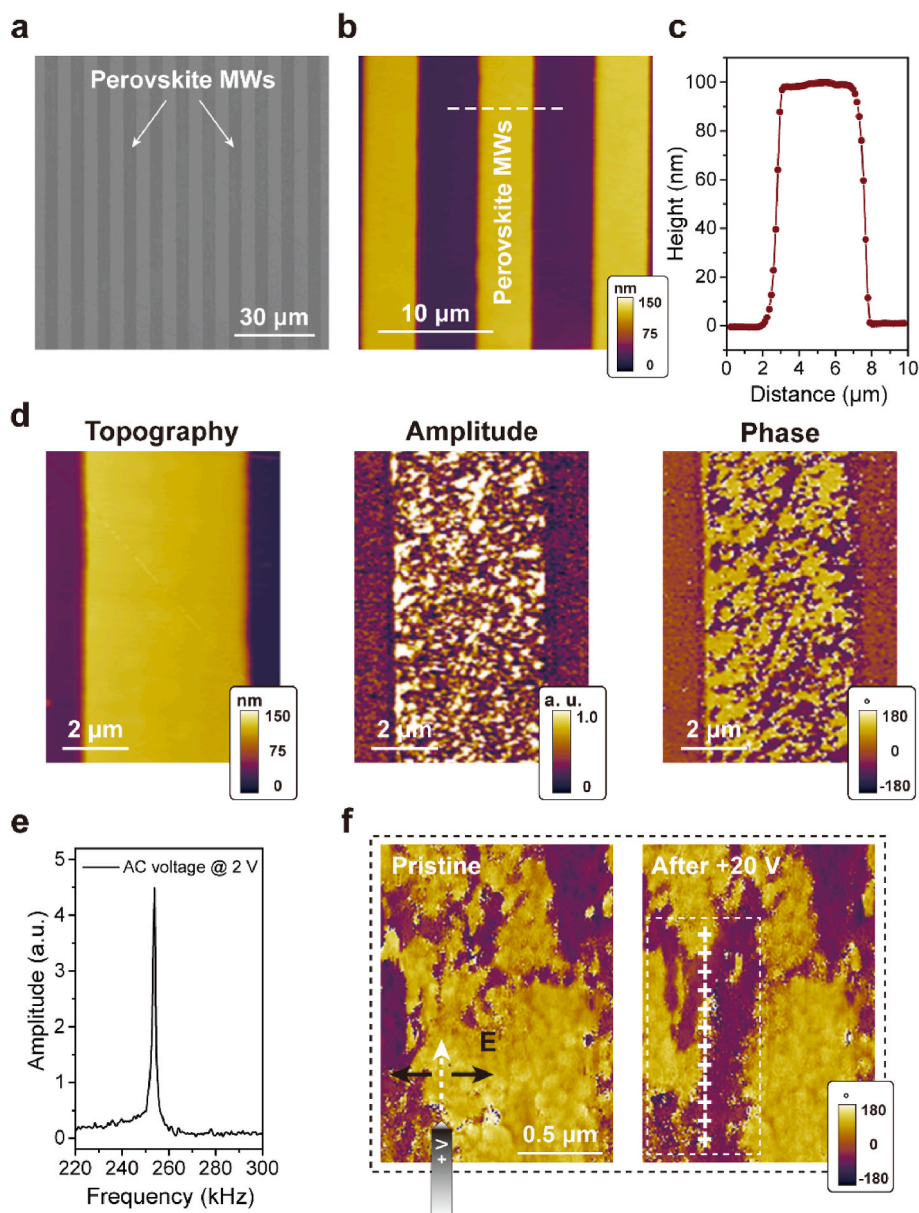

Fig. 2. (a) SEM image of the $(EA)_2(MA)_2Pb_3Br_{10}$ MWs. (b) AFM image and (c) the corresponding height profile of the $(EA)_2(MA)_2Pb_3Br_{10}$ MWs. (d) Topographic, amplitude and phase images of the $(EA)_2(MA)_2Pb_3Br_{10}$ MWs by lateral PFM. Randomly distributed ferroelectric domains are overlaid on top of an $(EA)_2(MA)_2Pb_3Br_{10}$ MW. (e) Lateral cantilever frequency response acquired from the $(EA)_2(MA)_2Pb_3Br_{10}$ MWs at an AC voltage bias of 2 V. (f) Polarization-switching behavior of the $(EA)_2(MA)_2Pb_3Br_{10}$ MWs obtained from lateral PFM phase images via a scanning biased probe.

decreases from 16 ($I4/mmm$) to 4 ($Cmc2_1$), indicating a biaxial feature of $(EA)_2(MA)_2Pb_3Br_{10}$ with four equivalent in-plane directions. Second harmonic generation (SHG) technique was employed to identify the non-centrosymmetric structure of $(EA)_2(MA)_2Pb_3Br_{10}$. Fig. S5 depicts that $(EA)_2(MA)_2Pb_3Br_{10}$ MWs are SHG-active at room temperature. The emerging SHG peak at 500 nm corresponds to the half wavelength of the 1000 nm laser excitation and provides solid evidence of the broken inversion symmetry in $(EA)_2(MA)_2Pb_3Br_{10}$. The Berry phase method was further used to evaluate the ferroelectric polarization of $(EA)_2(MA)_2Pb_3Br_{10}$. It is noted that both organic cations and metal-halide frameworks contribute to the ferroelectric polarization. We considered the substitution of EA^+ and MA^+ cations with K^+ at N^+ atomic positions, but keeping the $[PbBr_6]^{4-}$ octahedra positions of the relaxed structure. Details of the computational parameters used for the calculation can be found in the reference. [42] The polarization along in-plane direction was theoretically predicted to be about 2.28 $\mu C \, cm^{-2}$.

PFM measurements were then used to explore the nanoscale ferroelectric properties of $(EA)_2(MA)_2Pb_3Br_{10}$. Fig. 2d presents the topographic image as well as the corresponding lateral PFM amplitude and phase images overlaid on top of an $(EA)_2(MA)_2Pb_3Br_{10}$ MW. Noted that lateral PFM reflects the torsional motion of the AFM cantilever caused by the shear piezoelectric effect [43]. While in contact with the $(EA)_2(MA)_2Pb_3Br_{10}$ MWs, the lateral piezoresponse signal can be strongly detected at a frequency of around 250 kHz (Fig. 2c). Randomly distributed ferroelectric domains at the micrometer scale can be distinguished from the associated amplitude and phase images. Because of the zero polarization along vertical vector, there is no obvious domain textures shown in the corresponding vertical PFM images (Fig. S6). Clear domain walls of the $(EA)_2(MA)_2Pb_3Br_{10}$ MW can be found in Fig. S7 based on the distinct amplitude intensities and 180° phase contrast, which exhibit different domain orientations [44–46]. Meanwhile, the domains in Fig. S8 manifest three different color tones in phase contrast.

The multiaxial polarization directions of $(EA)_2(MA)_2Pb_3Br_{10}$ can be inferred from the probe scanning direction, which is in agreement with multiaxial feature of ferroelectric $(EA)_2(MA)_2Pb_3Br_{10}$ [44–46]. Switching characteristics of the ferroelectric domains are then investigated by applying a stray field from a biased AFM probe. As shown in Fig. 2f, the AFM probe was applied with a positive bias of 20 V and scanned along the dashed arrow. A so-called "trailing field" will be generated aside the probe movement to switch the proximate domains [47,48]. Most of the ferroelectric domains within the labelled region can be switched and shown in the opposite color tone as a function of the trailing field. Based on these observations, in-plane multiaxial merit of ferroelectricity is confirmed inside $(EA)_2(MA)_2Pb_3Br_{10}$ MWs, which may facilitate their operation in lateral-type devices.

The RP-type 2D layered architecture endows $(EA)_2(MA)_2Pb_3Br_{10}$ with great advantages, such as multiple quantum wells and dielectric confinement effect, which hold great promise for optoelectronic devices [49]. Herein, the investigation of optical properties of $(EA)_2(MA)_2Pb_3Br_{10}$ MWs was launched prior to the photodetector fabrication (Fig. 3a). KPFM was first used to examine the photoresponse of $(EA)_2(MA)_2Pb_3Br_{10}$ MWs by mapping out the surface potential. The dynamics of surface charge on semiconductors can be directly determined by the contact potential difference (CPD) between the AFM probe and the sample [50,51]. Fig. 3b exhibits the AFM image of $(EA)_2(MA)_2Pb_3Br_{10}$ MWs on the Pt-coated SiO_2/Si substrate and the corresponding KPFM images under dark and light illumination. As illustrated, there is a clear CPD contrast obtained between the $(EA)_2(MA)_2Pb_3Br_{10}$ MWs and the substrate. When photons are absorbed within $(EA)_2(MA)_2Pb_3Br_{10}$ MWs, excess hole-electron pairs will be generated and separated by the ferroelectric polarizations, producing a change in the surface potential [37,51]. Upon light illumination, the CPD underwent an apparent reduction from −450 mV to −550 mV due to the accumulated photogenerated charges on the MW surface. Fig. S9
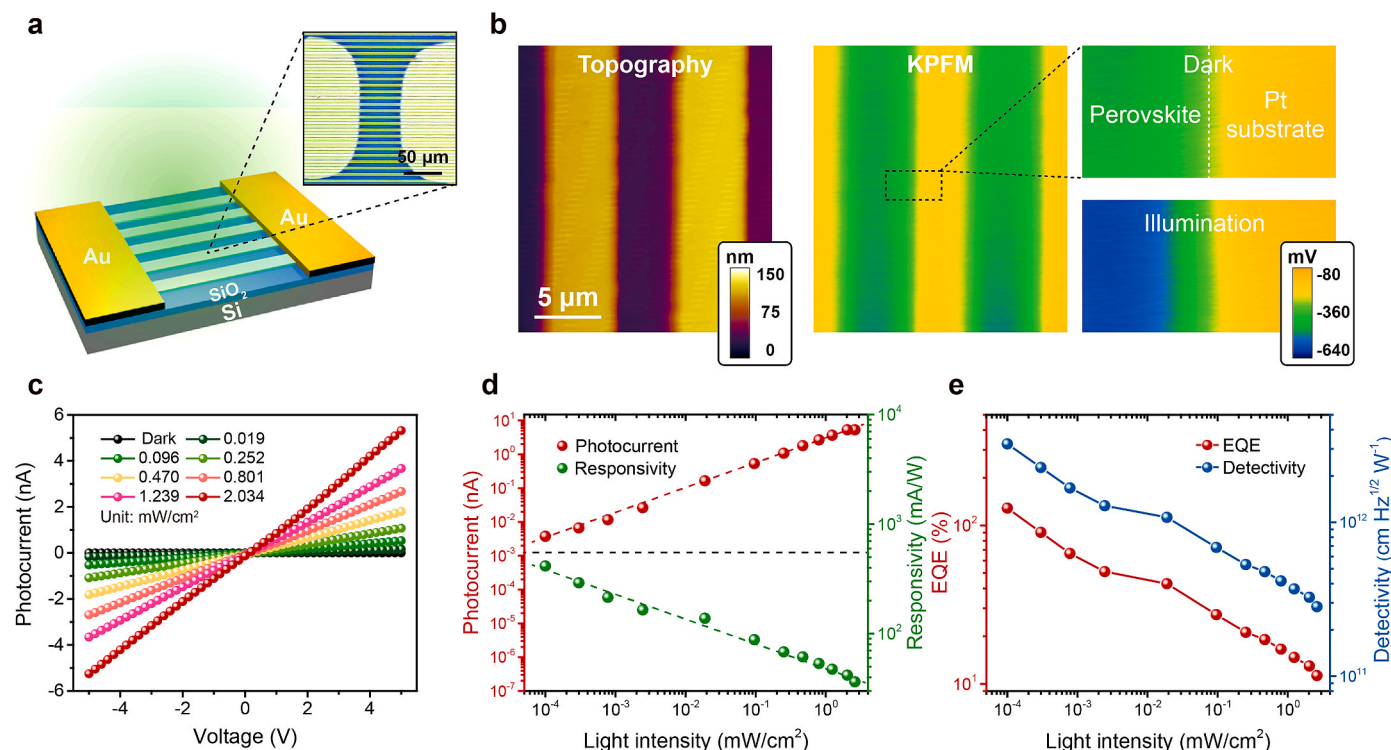

Fig. 3. (a) Schematic illustration of $(EA)_2(MA)_2Pb_3Br_{10}$ MWs-based photodetector. The inset is an enlarged optical image of active area. (b) Topographic and KPFM images of the $(EA)_2(MA)_2Pb_3Br_{10}$ MWs on Pt-coated SiO_2/Si substrate. The contact potential difference is obtained under dark and illumination conditions. (c) Photocurrent-voltage curves of the photodetectors measured under dark and light illuminations of 400 nm wavelength by varying light intensities. (d) Plots of photocurrent and responsivity of the photodetectors within the incident light intensities ranging from 1×10^{-4} to 2.61 mW cm^{-2} at 5 V bias. (e) The corresponding EQE and detectivity of the photodetectors.

shows the correlated KPFM profiles of Fig. 3b and the CPDs in both dark and light illumination exhibited a gradual potential transition. Due to the significant potential difference between the $(EA)_2(MA)_2Pb_3Br_{10}$ MWs and the substrate, there appears an obvious boundary under light illumination due to the yellow-green-blue color tone. This charge-separation process provides direct proof of $(EA)_2(MA)_2Pb_3Br_{10}$ MWs as the photon-sensitized substance for photodetection application.

Absorbance and photoluminescence (PL) spectra performed on $(EA)_2(MA)_2Pb_3Br_{10}$ MWs present an absorption cut-off at 497 nm and PL peak at 507 nm, of which the bandgap can be extracted to be 2.5 eV from the absorption edge (Fig. S10) [24]. Based on the density functional theory (DFT) calculations, the conduction band minimum (CBM) and valence band maximum (VBM) of $(EA)_2(MA)_2Pb_3Br_{10}$ coherently locate at the G point, indicating a direct bandgap feature for efficient electronic transition (Fig. S11). The partial density of states analysis discloses that the electronic structure near the Fermi level mainly originates from Pb 6p and Br 4p states (Fig. S12). To further confirm the electronic structure of $(EA)_2(MA)_2Pb_3Br_{10}$, ultraviolet photoelectron spectroscopy (UPS) measurement was employed. The VBM and CBM were determined to be −5.98 eV and −3.48 eV, respectively, as shown in Fig. S13. The PL decay curve of the $(EA)_2(MA)_2Pb_3Br_{10}$ MWs in Fig. S14 was also measured and fitted by a biexponential curve with a fast decay component (τ_1) of 6.52 ns and slow component (τ_2) of 42.3 ns. This long PL lifetime implies high crystallinity and suppressed trap states inside $(EA)_2(MA)_2Pb_3Br_{10}$ MWs [39,40]. As expected, single-crystalline $(EA)_2(MA)_2Pb_3Br_{10}$ MWs exhibit excellent photoresponse, moderate bandgap and long carrier lifetime, making them an ideal candidate for use in photodetection devices.

To evaluate the photodetection performance, $(EA)_2(MA)_2Pb_3Br_{10}$ MWs-based photodetectors were fabricated with a lateral-type structure of Au/MWs/Au by E-beam thermal evaporation through a shadow mask. As shown in Fig. 3a, the prototype photodetector exhibits an effective illumination area of about 6.25×10^{-5} cm^2 across a bridging-gap width of 50 μm. The photoresponse characteristics of the $(EA)_2(MA)_2Pb_3Br_{10}$ MWs-based photodetectors were examined by measuring the photocurrent-voltage curves under dark and light illumination of 400 nm with various light intensities (Fig. 3c). The linear curves indicate an ohmic contact between $(EA)_2(MA)_2Pb_3Br_{10}$ MWs and Au electrodes. Responsivity (R) represents the generation ratio of photocurrent as a function of illumination intensity, which can be defined as [52–54].

$$R = \frac{I_{light} - I_{dark}}{P \times A} \qquad (1)$$

where I_{light} and I_{dark} are the photocurrent and dark current, respectively, obtained at 5 V bias, P is the incident light intensity, and A is the active area of the photodetector. As shown in Fig. 3d, both photocurrent and responsivity show a linear power relationship with the increasing incident light intensities from 1×10^{-4} to 2.61 mW cm^{-2}. The maximum value of responsivity is obtained to be 415 mA W^{-1} at the lowest intensity of 1×10^{-4} mW cm^{-2}, and it gradually decays with the increasing intensity due to the sign of trapped photogenerated carriers in $(EA)_2(MA)_2Pb_3Br_{10}$ MWs, which was usually observed in photoconductive detectors based on hybrid perovskites [52–54]. At low light intensity, photogenerated carriers will be captured by deep traps, resulting in a longer carrier lifetime and hence higher responsivity. When the light intensity increases, deep traps tend to be filled and photogenerated carriers will be captured by shallower ones. In this case, the decreased carrier lifetime leads to the decay of the responsivity, which is the so-called dynamic-range enhancing gain compression. Another two key figure-of-merits, spectral detectivity (D^*) and external quantum efficiency (EQE), can be estimated based on the following equations [52–54].

$$D^* = \frac{(Af)^{1/2}R}{\overline{i_n^2}^{1/2}} \qquad (2)$$

$$EQE = \frac{Rhc}{q\lambda} \qquad (3)$$

where f is the bandwidth, R is the obtained responsivity, and h, c, q and λ are Planck's constant, the velocity of light, the electronic charge, and the wavelength of incident light, respectively. The $\overline{i_n^2}^{1/2}$ is the root mean square value of the noise current that can be extracted from the dark current operated at 5 V bias (Fig. S15a). The low dark current at the level of $\sim 10^{-13}$ A signifies the high crystallinity and suppressed trap states of $(EA)_2(MA)_2Pb_3Br_{10}$ MWs, which provides a low noise level for achieving a high detectivity. After performing Fourier transform (FFT) of the measured dark current, the noise level per unit bandwidth (1 Hz) of the $(EA)_2(MA)_2Pb_3Br_{10}$ MWs-based photodetectors was estimated to be $\sim 1.013 \times 10^{-15}$ A Hz$^{-1/2}$ (Fig. S15b) [55,56]. Light-intensity-dependent D^* and EQE of $(EA)_2(MA)_2Pb_3Br_{10}$ MWs-based photodetectors are plotted in Fig. 3e. The maximum value of D^* and EQE can be calculated to be about 3.23×10^{12} cm Hz$^{1/2}$ W^{-1} (Jones) and 129% at the incident light of 400 nm. These results imply that single-crystalline $(EA)_2(MA)_2Pb_3Br_{10}$ MWs with perfect crystallographic orientation and semiconducting features are superior for photodetection application.

Intrigued by their in-plane biaxial ferroelectricity and excellent photodetection performance, we set out to scrutinize the photovoltaic behavior on the $(EA)_2(MA)_2Pb_3Br_{10}$ MWs-based photodetectors. Prior to the investigation, an electrical-poling process was conducted on the photodetectors by applying a constant bias pulse for a period of poling time (See details in experimental section) [24–27]. After a forward high-field poling of +2 V/μm, an open-circuit voltage (V_{oc}) and a short-circuit current (I_{sc}) can be observed while exposed to light illumination. As shown in Fig. 4a, the V_{oc} was fixed at 0.48 V and the zero-bias I_{sc} gradually increased with the increasing light intensities. On reaching the intensity of 2.61 mW cm^{-2}, the I_{sc} achieved a maximum value of ~ 0.15 nA at the zero bias (Fig. 4b). Under identical measuring condition (i.e., intensity of 2.61 mW cm^{-2} and bias at 0 V), the time-dependent I_{sc} in the light "on/off" cycles displayed an obvious change by three orders of magnitude (Fig. S16a), indicating a promising self-powered photoactive behavior [24–27]. Upon the electrical-poling treatment, the temporal photocurrent response of the photodetectors exhibited an apparent shortening in both rise and decay time. The rise time is defined as the time interval for the response to rise from 10% to 90% of its saturated value, and the decay time is the opposite fall from 90% to 10% [52–54]. As shown in Fig. 4c, the rise time sped up to 28 ms after poling, in contrast to the 38 ms without poling, and the decay time showed a decrease from 62 ms to 51 ms. We further examined the switching photovoltaics by subjecting the photodetectors to a reverse poling of −2 V/μm. As shown in Fig. 4d, the direction of both V_{oc} and I_{sc} can be reversed by the inverting electric poling, whereas the magnitude of V_{oc} and I_{sc} remains the same. The tunable V_{oc} and I_{sc} together with the accelerated response time signify that the fundamental understanding of this photovoltaic behavior is of great significance in achieving high-performance self-powered devices [24–27].

With respect to the switchable photoelectric responses, there are two relevant factors, namely ion migration and ferroelectric photovoltaic effect that need to be considered. Ion migration and associated ion accumulation have been proposed to introduce space-charge doping in proximity of the electrodes, thus forming a p-i-n device structure after electrical poling [28–31]. To identify the possible effect of ion migration, we subjected the $(EA)_2(MA)_2Pb_3Br_{10}$ MWs-based photodetectors to a dynamic poling process as a function of different poling electric fields. It can be quantified by monitoring the typical time-dependent I_{sc} curves of the photodetectors in the "on/off" cycles at zero bias under the light intensity of 2.61 mW cm^{-2}. The non-poled photodetector was measured as a reference and exhibited a steady-state I_{sc} with a limited photocurrent value of about −0.01 nA (Fig. 5a). This zero-bias photocurrent response has a preferential directionality, which is closely related to the
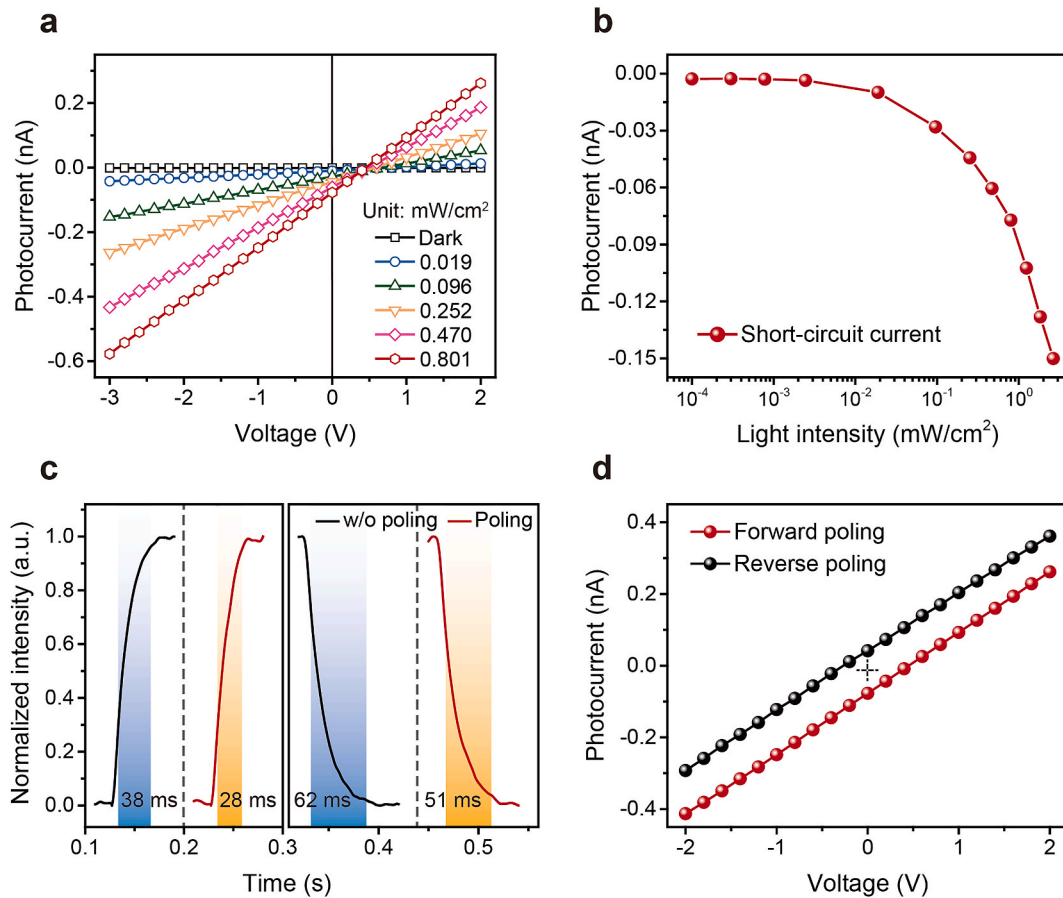
Fig. 4. (a) Photocurrent density dependence of voltage bias for high-electric-field poled photodetectors, showing an apparent open-circuit voltage and short-circuit current. (b) The short-circuit currents under different light intensities. (c) Temporal response of the photodetectors without poling and after a forward poling, showing a shortened rise and decay time. (d) Photocurrent-voltage curves with the inversion of polarized direction.

in-plane spontaneous polarization inside $(EA)_2(MA)_2Pb_3Br_{10}$ MWs. Interestingly, a depressed I_{sc} was seen at first while applying a low-field reverse poling of -0.1 V/μm, and gradually recovered to the initial current level of around -0.01 nA, as shown in Fig. 5b. When the poling electric field was set to be -0.2 V/μm, the direction of I_{sc} changed to the opposite together with a current up to $+0.005$ nA. It is known that the photocurrent consists of drift current and diffusion current [57,58]. Drift current is a flow of charge carriers driven by the build-in electric field which is mainly caused by the ferroelectric polarization inside the $(EA)_2(MA)_2Pb_3Br_{10}$ MWs. And, the diffusion current comes from the gradient distribution of charged ions of vacancies. Carriers will diffuse from high-density areas to low-density regions, forming the so-called diffusion current. After poled at -0.2 V/μm, ion charges will freely drift close to the electrodes resulting in a high gradient distribution of charges and consequently a large diffusion current. The reverse poling makes the direction of diffusion current opposite to the drift current. When the diffusion current is larger than the drift current, the direction of I_{sc} from the photodetectors changes to the opposite. Upon the extension of the measuring time, I_{sc} flipped back and returned to the initial state again (Fig. 5c), suggesting that the poling effect can be relaxed as the ions diffused back [59]. These observations substantiate that ion-migration effects play a key role in modulating the device performance [28–31]. According to previous reports, the poling electric field is required to be higher than 0.3 V/μm, which can trigger ions to accumulate near the electrodes and induce a doping effect [29]. On the other hand, the high-field poling electric field enables to control the orientation of the ferroelectric polarization of $(EA)_2(MA)_2Pb_3Br_{10}$ to be aligned along the electric field. As shown in Fig. 5d, the I_{sc} exhibited a strong response to the high-electric-field poling of -2 V/μm, including a

reversed direction and an enhanced photocurrent up to $+0.15$ nA. The stable reverse photocurrent implies that the extension of measuring time exerted little influence on the poling effect.

To verify this scenario, we mapped the local surface electrical potential of $(EA)_2(MA)_2Pb_3Br_{10}$ MWs close to the Au electrodes using KPFM measured in dark. The ion migration has been demonstrated to induce space-charge doping in the perovskite film, giving rise to a change of surface potential [28–31]. On the basis of the previous investigations, the accumulation of the negatively charged ions or vacancies was predicted to induce p-type doping, whereas positively charged ions or vacancies result in n-type doping [28–30]. The KPFM probe scanned across the $(EA)_2(MA)_2Pb_3Br_{10}$ MWs and Au cathode with an area of 10 μm × 20 μm, where the Au was used as a reference. The schematic of the KPFM measurement is shown in Fig. 5e. After high-field poling of -0.2 V/μm, the CPD of the $(EA)_2(MA)_2Pb_3Br_{10}$ MW shows no obvious potential change in comparison to that of non-poled MW, as shown in Fig. 5f. However, a striking contrast of CPD can be observed from KPFM images after a high-field poling, indicating ion accumulation occurring in proximity of the cathode. The CPD of the high-electric-field poled MW exhibited a reduction of ~100 mV in surface potential at reverse poling of -2 V/μm, whereas an increase of ~140 mV at forward poling of $+2$ V/μm (Fig. 5g). According to the KPFM measurements by Asylum Research MFP-3D Infinity, the CPD can be defined as [50,51].

$$CPD = \frac{\varphi_{probe} - \varphi_{sample}}{e} \qquad (4)$$

where φ_{sample} is the surface potential of the sample, φ_{probe} is the work function of the Pt/Ir-coated probe, and e is the electronic charge. Such a reduction or an increase of CPD coincide with the assumption of n-type
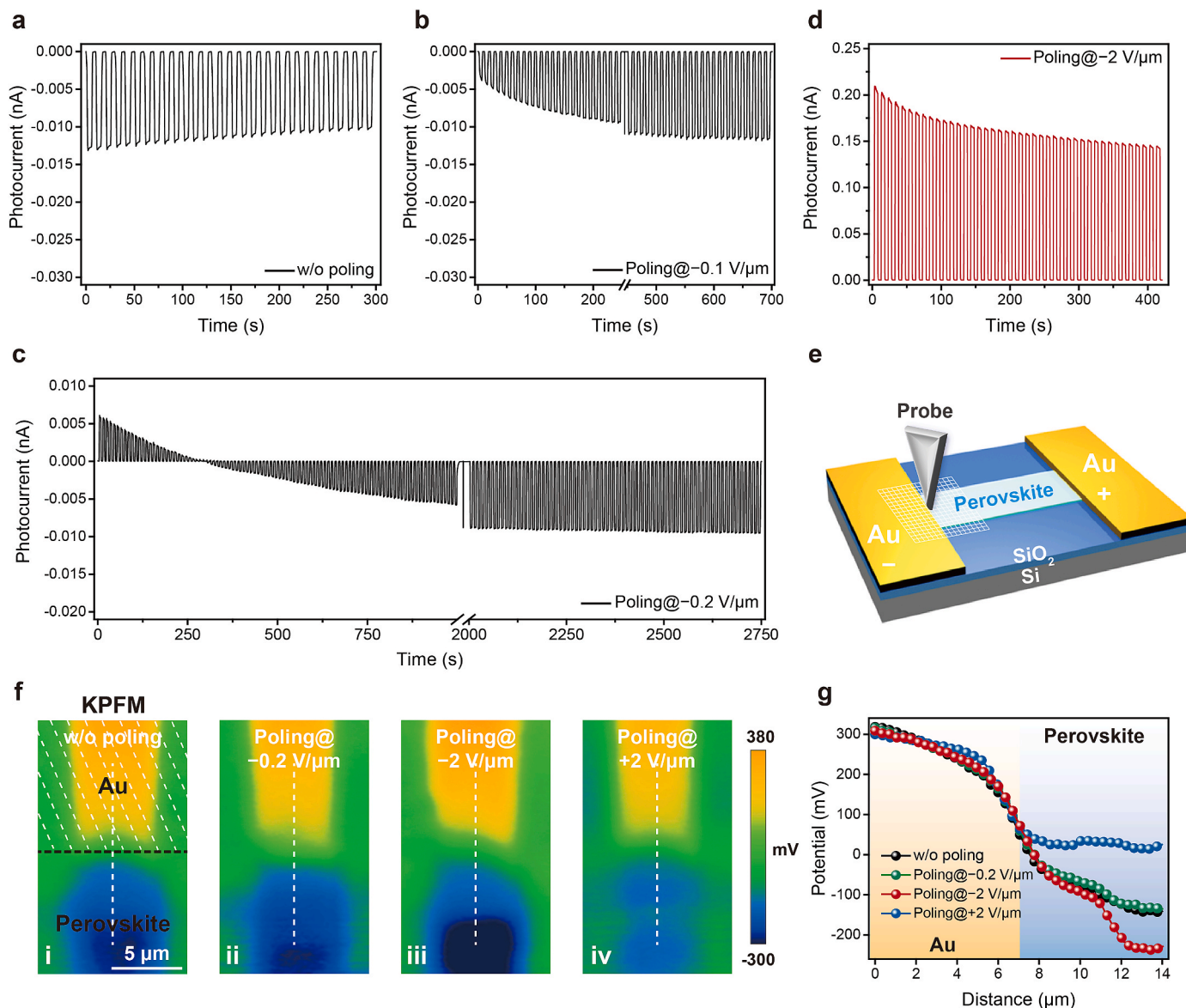
Fig. 5. Time-dependent photocurrent response of photodetectors with periodic on/off illumination under zero bias (a) before poling, and after different electric-field poling treatment of (b) reverse poling at -0.1 V/μm, (c) reverse poling at -0.2 V/μm, and (d) reverse poling at -2 V/μm. (e) Schematic of the KPFM measurements of the lateral $(EA)_2(MA)_2Pb_3Br_{10}$ MWs-based photodetectors, where the white grid lines indicate the scanning region of about 10 μm × 20 μm. (f) KPFM potential images of the $(EA)_2(MA)_2Pb_3Br_{10}$ MWs at the perovskite/Au electrode interface i) before poling, and after different electric-field poling treatment of ii) reverse poling at -0.2 V/μm, iii) reverse poling at -2 V/μm, and iv) reverse poling at $+2$ V/μm. (g) Correlated KPFM potential profiles along the dash lines denoted in (f).

or p-type doping in the vicinity of the cathode, resulting in the increase and decrease of the surface potential of the $(EA)_2(MA)_2Pb_3Br_{10}$ MWs [28–31]. Besides the ion migration, the ferroelectric polarization switching is also investigated by PFM after a high-electric-field poling. As above validated in PFM measurements, ferroelectrics are endowed with spontaneous polarization that can be switched under an external electric field [20]. From the structural point of view, ferroelectric polarization of $(EA)_2(MA)_2Pb_3Br_{10}$ arises from the horizontal off-center ordering of bulky spacer EA^+ cations with respect to the trilayered inorganic $[PbBr_6]^{4-}$ octahedra, which is confined within the vdW gaps along the in-plane direction, and contributes to the separation and transport of polarization-related photogenerated carriers (Fig. S17) [20, 24]. Starting with the non-poled $(EA)_2(MA)_2Pb_3Br_{10}$ MWs, irregular ferroelectric domains with different polarization directions can be clearly observed from the lateral PFM phase image, as shown in Fig. 6a. After high-field poling at $+2$ V/μm, the local polarization switching happened over the MWs and the polarization direction tended to be

aligned along the applied electric field. Remarkably, the enlarged PFM amplitude and phase images strongly support the polarization reversal by the changed domain textures (Fig. 6b). The correlated PFM phase profile also confirmed the polarization switching by the phase signal change of 180°, as shown in Fig. 6c.

Taking together these observations, we ascribe this photovoltaic behavior to the coupling of ion migration and ferroelectric photovoltaic effect under the electrical poling in the $(EA)_2(MA)_2Pb_3Br_{10}$ MWs-based photodetectors. Upon a low-field poling, the electric field is not high enough to trigger ions to accumulate near the perovskite/electrode interface, or even align the ferroelectric polarization of $(EA)_2(MA)_2Pb_3Br_{10}$ (Fig. 6d). Therefore, ion charges will freely drift inside the $(EA)_2(MA)_2Pb_3Br_{10}$ MWs and gradually diffuse back under the driving force of random spontaneous polarization, resulting in the relaxation of the poling effect. However, the high-electric-field poling is able to drive the oppositely charged ions to accumulate in the vicinity of the electrodes and induce the space-charge doping. Meanwhile, random
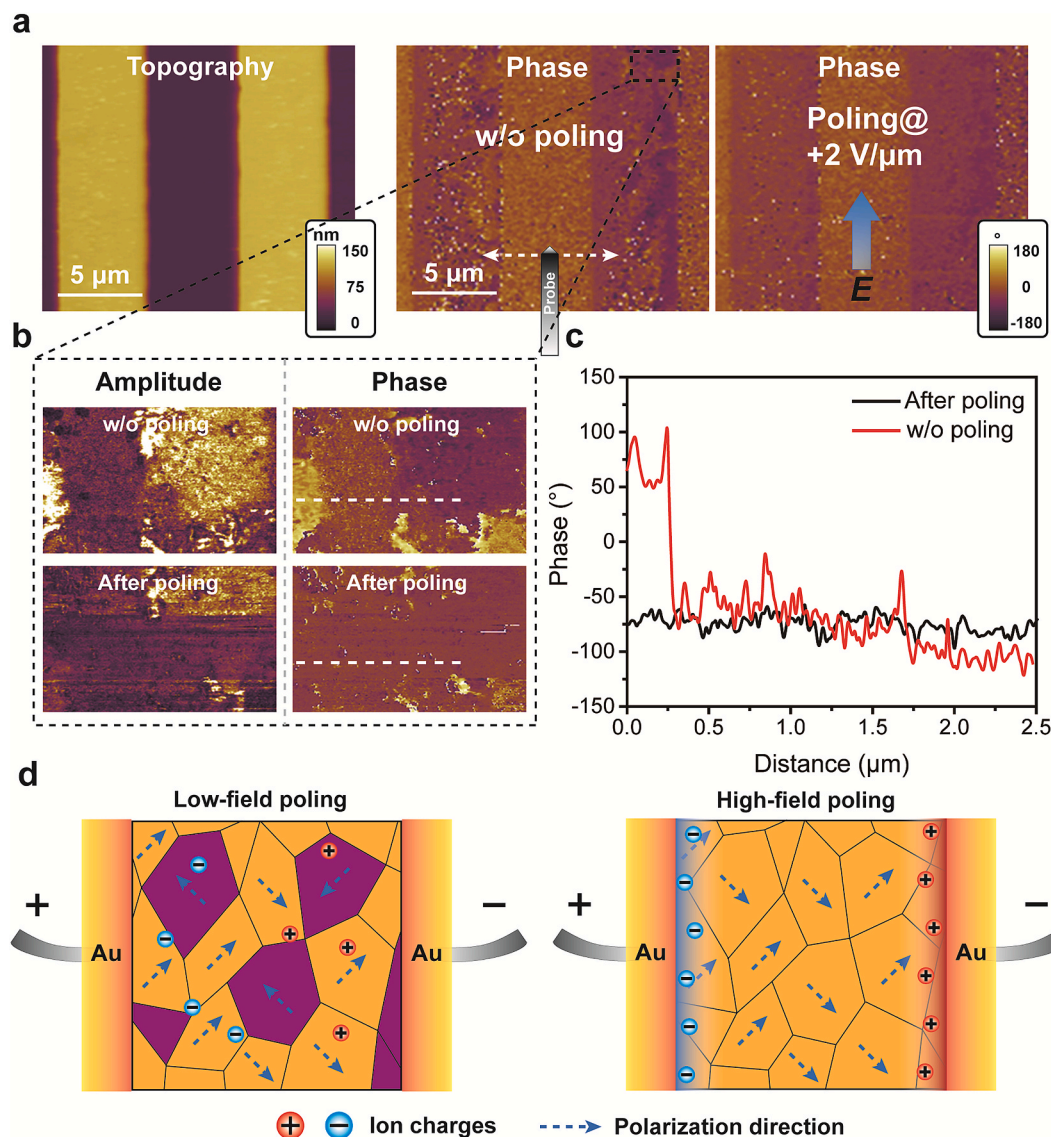
Fig. 6. (a) Lateral PFM images of the polarization switching overlaid on the $(EA)_2(MA)_2Pb_3Br_{10}$ MWs-based photodetectors by using the scanning probe. The $(EA)_2(MA)_2Pb_3Br_{10}$ MWs-based photodetector was poled by a high-field poling of +2 V/μm. (b) Lateral PFM amplitude and phase images before and after poling. (c) Correlated PFM phase profiles along the dash lines denoted in (b). (d) Schematics of ion migration and ferroelectric polarization switching in $(EA)_2(MA)_2Pb_3Br_{10}$ MWs during low-field and high-field poling, respectively.

spontaneous polarization of $(EA)_2(MA)_2Pb_3Br_{10}$ can be switched in response to the high-field poling and tend to be aligned along the electric field. The dynamic reorientation of organic cations and tilting motions of inorganic framework offer support to the origin of this ferroelectric polarization switching, as shown in Fig. S16 [24]. As a consequence, both doping-induced potential drop and ferroelectric polarization-dependent activity provide a driving force for the separation and flipping of photogenerated carriers, which are responsible for the enhancement, switchability and accelerated response time of I_{sc} and V_{oc}. Based on such electric-field-induced effects and excellent photodetection performance, $(EA)_2(MA)_2Pb_3Br_{10}$ MWs could behave as a promising candidate for high-performance self-powered photodetectors. Specifically, the highest short-circuit current density can be estimated to be ~1.2 mA cm^{-2} under the light intensity of 2.61 mW cm^{-2} (Fig. S16b), which is larger than that of most ferroelectric oxide and even superior to the reported ferroelectric perovskite bulk crystals. It can be ascribed to the excellent single-crystallinity of $(EA)_2(MA)_2Pb_3Br_{10}$ MWs with low trap density, which have suppressed the undesirable carrier scattering and trapping. Meanwhile, the well-aligned microwire arrays with

confined thickness will support an efficient in-plane exciton transport for achieving high photocurrent density. The photodetection figures-of-merit compared with those of previously reported self-powered photodetectors based on ferroelectric materials are summarized in Table S1.

4. Conclusions

In summary, we have demonstrated a template-assisted space-confined method for the growth of well-aligned single-crystalline $(EA)_2(MA)_2Pb_3Br_{10}$ MWs, which yielded perfect crystallinity and well control of thickness at the nanoscale. The in-plane multiaxial ferroelectricity of $(EA)_2(MA)_2Pb_3Br_{10}$ was investigated by PFM measurements, and randomly distributed domain textures can be observed over the $(EA)_2(MA)_2Pb_3Br_{10}$ MWs. A comprehensive set of characteristics, including SHG signal, domain walls, and domain switchability, further confirmed the ferroelectric nature within $(EA)_2(MA)_2Pb_3Br_{10}$ MWs. Together with their desirable photodetection performance, $(EA)_2(MA)_2Pb_3Br_{10}$ MWs-based photodetectors provided a good

platform to exploit the photovoltaic behavior of perovskite ferroelectrics and expand the application to self-powered photodetectors, attaining accelerated response time and switchable photoelectric responses with high current density ($\sim$1.2 mA cm^{-2}), which is much higher than that found in the most active ferroelectric oxide. The comprehensive study of the dynamic poling process for the photodetectors, including electrical-poling-dependent photocurrent, KPFM mapping and ferroelectric polarization switching, has experimentally supported the findings that the coupling of ion migration and ferroelectric photovoltaic effect should be responsible for the photovoltaic behavior in perovskite ferroelectrics. This work provides a new insight for understanding the origin of photovoltaic behavior in hybrid perovskite ferroelectrics, which will open up new applications for the area of self-powered electronics.

Author contributions

Ran Ding: Conceptualization, Methodology, Software, Writing-original draft preparation. **Yongxin Lyu**: Software, Data curation, Writing-original draft preparation. **Yuqian Zhao**: Methodology, Investigation. **Zehan Wu**: Investigation. **Feng Guo**: Methodology, Investigation. **Weng Fu Io**: Investigation. **Sin-Yi Pang**: Investigation. **Jianfeng Mao**: Investigation. **Man-Chung Wong**: Investigation. **Lok Wing Wong**: Investigation. **Cenqi Yan**: Investigation. **Jiangsheng Yu**: Investigation. **Jiong Zhao**: Validation. **Gang Li**: Validation. **Jianhua Hao**: Validation, Supervision, Writing- Reviewing and Editing, Project administration, Funding acquisition.

Declaration of competing interest

The authors declare that they have no known competing financial interests or personal relationships that could have appeared to influence the work reported in this paper.

Data availability

Data will be made available on request.

Acknowledgements

Appendix A. Supplementary data

Supplementary data to this article can be found online at https://doi.org/10.1016/j.mtphys.2022.100867.

References

[1] A.M. Glass, et al., Appl. Phys. Lett. 25 (1974) 233–235.
[2] W. Koch, et al., Solid State Commun. 17 (1975) 847–850.
[3] P. Brody, et al., J. Electron. Mater. 4 (1975) 955–971.
[4] T. Choi, et al., Science 324 (2009) 63–66.
[5] S.Y. Yang, et al., Nat. Nanotechnol. 5 (2010) 143–147.
[6] M. Alexe, et al., Nat. Commun. 2 (2011) 256.
[7] L. You, et al., Sci. Adv. 4 (2018): eaat3438.
[8] W. Ji, et al., Adv. Mater. 22 (2010) 1763–1766.
[9] B. Cui, et al., Nat. Commun. 13 (2022) 1707.
[10] S. Cheng, et al., iScience 23 (2020): 101874.
[11] G.C. Xing, et al., Science 342 (2013) 344–347.
[12] S.D. Stranks, et al., Science 342 (2013) 341–344.
[13] Q. Dong, et al., Science 347 (2015) 967–970.
[14] D. Shi, et al., Science 347 (2015) 519–522.
[15] S. Chen, et al., Adv. Mater. 29 (2017): 1605448.
[16] C.C. Stoumpos, et al., Chem. Mater. 28 (2016) 2852–2867.
[17] G. Grancini, et al., Nat. Rev. Mater. 4 (2019) 4–22.
[18] W. Zhang, et al., Chem. Rev. 112 (2012) 1163–1195.
[19] W.Q. Liao, et al., Nat. Commun. 6 (2015) 1–7.
[20] L. You, et al., Adv. Mater. 30 (2018): 1803249.
[21] R. Ding, et al., EcoMat. 2 (2020): e12057.
[22] S. Shahrokhi, et al., Small Methods 4 (2020): 2000149.
[23] S. Wang, et al., J. Am. Chem. Soc. 141 (2019) 7693–7697.
[24] X. Liu, et al., Angew. Chem., Int. Ed. 58 (2019) 14504–14508.
[25] S. Wang, et al., J. Am. Chem. Soc. 142 (2020) 55–59.
[26] I. Park, et al., J. Am. Chem. Soc. 142 (2020) 18592–18598.
[27] S. Han, et al., Nat. Commun. 12 (2021) 284.
[28] Z. Xiao, et al., Nat. Mater. 14 (2015) 193–198.
[29] Y. Yuan, et al., Adv. Energy Mater. 5 (2015): 1500615.
[30] Y. Yuan, et al., Adv. Energy Mater. 6 (2015): 1501803.
[31] J. Huang, et al., Nat. Rev. Mater. 2 (2017): 17042.
[32] Z. Chen, et al., Nat. Commun. 8 (2017) 1890.
[33] Y. Liu, et al., Nat. Commun. 9 (2018) 5302.
[34] W. Yu, et al., Nat. Commun. 9 (2018) 5354.
[35] R. Ding, et al., Adv. Mater. 33 (2021): 2101263.
[36] R. Ding, et al., Nano Lett. 20 (2020) 2747–2755.
[37] J. Feng, et al., Nat. Electron. 1 (2018) 404–410.
[38] Y. Zhao, et al., J. Am. Chem. Soc. 143 (2021) 8437–8445.
[39] W. Deng, et al., Adv. Mater. 28 (2016) 2201–2208.
[40] W. Deng, et al., Adv. Mater. 32 (2020): 1908340.
[41] K. Aizu, J. Phys. Soc. Jpn. 27 (1969) 387–396.
[42] R.D. King, et al., Phys. Rev. B 47 (1993) 1651–1654.
[43] T. Li, et al., Adv. Mater. 30 (2018): 1803064.
[44] P. Shi, et al., J. Am. Chem. Soc. 139 (2017) 1319–1324.
[45] P. Shi, et al., J. Am. Chem. Soc. 141 (2019) 18334–18340.
[46] H. Zhang, et al., J. Am. Chem. Soc. 143 (2021) 1664–1672.
[47] A. Crassous, et al., Nat. Nanotechnol. 10 (2015) 614–618.
[48] T.T. Sha, et al., Adv. Mater. 31 (2019): 1901843.
[49] K. Leng, et al., Nat. Rev. Mater. 5 (2020) 1–19.
[50] W. Melitz, et al., Surf. Sci. Rep. 66 (2011) 1–27.
[51] P. Zhao, et al., J. Phys. Chem. Lett. 6 (2015) 2622–2628.
[52] C. Xie, et al., Adv. Funct. Mater. 29 (2019): 1903907.
[53] H. Wang, et al., Chem. Soc. Rev. 46 (2017) 5204–5236.
[54] M. Ahmadi, et al., Adv. Mater. 29 (2017): 1605242.
[55] C. Xie, et al., Light Sci. Appl. 6 (2017): e17023 e17023.
[56] C. Liu, et al., Nat. Nanotechnol. 9 (2014) 273–278.
[57] J. Xing, et al., Appl. Phys. Lett. 106 (2015): 033504.
[58] A.B. Swain, et al., Apl. Mater. 7 (2019): 011106.
[59] C. Lan, et al., Adv. Mater. 32 (2020): 2005481.
[60] P. Giannozzi, et al., J. Phys. Condens. Matter 21 (2009): 395502.
[61] J.P. Perdew, et al., Phys. Rev. Lett. 78 (1996) 1396.
[62] S. Grimme, J. Comput. Chem. 27 (2006) 1787–1799.
[63] H.J. Monkhorst, et al., Phys. Rev. B 13 (1976) 5188–5192.